Chinese Chemical Letters 32 (2021) 1101–1105

Contents lists available at ScienceDirect

Chinese Chemical Letters

journal homepage: www.elsevier.com/locate/cclet

Communication

Deformable double-shelled hollow mesoporous organosilica nanocapsules: A multi-interfacial etching strategy

Zhihao Feng[a], Zhaogang Teng[a,*], Yuyuan Shi[b], Wenhui Shi[a], Xiaodan Su[a], Guangming Lu[c], Lianhui Wang[a], Lixing Weng[b,*]

[a] Key Laboratory for Organic Electronics & Information Displays and Jiangsu Key Laboratory for Biosensors, Institute of Advanced Materials, Jiangsu National Synergetic Innovation Centre for Advanced Materials, Nanjing University of Posts and Telecommunications (NJUPT), Nanjing 210023, China
[b] College of Geography and Biological Information, Nanjing University of Posts and Telecommunications, Nanjing 210046, China
[c] Department of Medical Imaging, Jinling Hospital, School of Medicine, Nanjing University, Nanjing 210002, China

ARTICLE INFO

Article history:
Received 25 June 2020
Received in revised form 29 July 2020
Accepted 31 July 2020
Available online 22 August 2020

Keywords:
Hollow structure
Mesoporous
Double-shelled
Organosilica
Anticancer

ABSTRACT

Multishelled hollow structures have drawn increasing interest because of their peculiar compartmentation environments and physicochemical properties. In this work, deformable double-shelled hollow mesoporous organosilica nanocapsules (DDHMONs) were successfully synthesized by a multi-interfacial etching strategy. The obtained DDHMONs have a double-shelled structure with aninorganic-organic hybrid framework, a uniform outer layer (~320 nm) and inner layer (~180 nm), ordered mesochannels (~2.21 nm), and a large specific surface area (~1233 m^2/g). *In vitro* toxicity tests show that the DDHMONs have excellent biocompatibility when coincubated with human breast cancer cells. In addition, the anticancer substance doxorubicin (DOX) can be highly loaded in DDHMONs (~335 μg/mg). The results from flow cytometry together with confocal laser scanning microscopy show that DOX can be efficiently delivered into MCF-7 cells by DDHMONs, thus improving chemotherapeutic efficiency and demonstrating that DDHMONs have potential nanomedicine applications as anticancer agents.

Multishelled hollow materials have recently become highly studied because they have multiple heterogeneous interfaces and compartmentation environments; furthermore, multishelled hollow materials have excellent physicochemical characteristics such as enhanced catalytic activity, prolonged drug release and high storage capacity [1–14]. Due to these attractive advantages, massive efforts have been invested to synthesize particles with hollow structures and multiple shells [15–24].

Previously, inorganic materials have been employed as raw materials, namely, metals or metal oxides to synthesize multishelled hollow structures. For example, ZnO and Co_3O_4 have been used to synthesize multishelled hollow particles through the thermal decomposition of coordination polymer particles containing metal ions [25]. In addition to thermal decomposition, the templating approach is another method to synthesize multishelled hollow nanoparticles. For instance, Jang and coworkers reported TiO_2 hollow particles with controllable numbers of shells synthesized by the hard templating method [26]. Lou *et al.* used a hydrothermal deposition method to synthesize hollow nanospheres with multiple shells [27]. However, all the shells of the multishelled nanoparticles described above are based on inorganic substances, causing their structures to exhibit hard properties. As far as we know, in the domain of drug delivery, rigid materials are difficult for cells to capture, which limits their potential applications [28]. Therefore, it is imperative to find a method to prepare a multishelled nanoparticle with soft shells.

Hollow mesoporous organosilica nanoparticles can be synthesized through hard templating or soft templating methods. Mesoporous organosilica nanoparticles show potential for application in many areas due to their advantages, such as accessible and orderly mesopores, large surface areas, and adjustable mechanical properties [29–34]. Teng *et al.* found that with extended reaction time, mesoporous organosilica nanoparticles could form a highly condensed surface and self-transform to nanoparticles with hollow structures. Mesoporous organosilica nanospheres with multiple highly condensed interfaces were prepared through cetyltrimethylammonium bromide (CTAB)-directed sol-gel processes by the continuous growth of mesostructured organosilica spheres. After hydrothermal treatment, mesoporous organosilica nanospheres with uniform multishelled hollow structures could be obtained [35]. However, the obtained

* Corresponding authors.
E-mail addresses: iamzgteng@njupt.edu.cn (Z. Teng), lxweng@njupt.edu.cn (L. Weng).

https://doi.org/10.1016/j.cclet.2020.08.023
1001-8417/

multishelled hollow nanospheres still did not possess deformability. Recently, we took advantage of the Stöber method, together with alkali etching, to successfully synthesize organosilica nanospheres with well-defined mesopores and deformable structures [36]. Inspired by the works above, we combined the multiple growth procedure with alkaline etching to obtain deformable multishelled mesoporous organosilica nanospheres.

Herein, monodisperse deformable double-shelled hollow mesoporous organosilica nanocapsules (DDHMONs) have been successfully prepared by a multi-interfacial etching strategy. This strategy includes the continuous formation of mesostructured organosilica nanospheres through a structural directing agent (SDA) directed sol-gel procedure followed by one-step etching with sodium hydroxide, during which solid nanospheres are transformed into nanocapsules with two soft shells. The obtained DDHMONs possess a unique deformable double-shelled structure, as well as inorganic-organic hybrid frameworks with a highly uniform outer layer diameter (~320 nm) and inner layer diameter (~180 nm), ordered mesochannels (~2.21 nm), a large superficial area (~1233 m^2/g) and a large pore volume (~1.63 cm^3/g). Furthermore, we found that DDHMONs demonstrate outstanding biocompatibility and can load and efficiently deliver the anticancer drug DOX (~335 μg/mg) to kill human breast cancer cells, suggesting that DDHMOs are promising in nanotherapeutic areas.

The following reagents were used in the experimental part of this work: Tetraethyl orthosilicate (TEOS), aqueous ammonia solution ($NH_3 \cdot H_2O$, 25 wt%), solid sodium hydroxide (NaOH), concentrated hydrochloric acid (HCl, 37 wt%) and CTAB were obtained from Sinopharm Chemical Reagent Co., Ltd. (Shanghai, China). Anhydrous ethanol was obtained from Nanjing Chemical Reagent Co., Ltd. (Nanjing, China). 1,2-Bis(triethoxysilyl)ethane (BTSE) was obtained from Sigma-Aldrich (St. Louis, Missouri, USA). A cell counting kit-8 (CCK-8) along with phosphate-buffered saline (PBS) solution and RPMI-1640 medium were purchased from Keygen Biotechnology Co., Ltd. (Nanjing, China). 4,6-Diamidino-2-phenylindole (DAPI) was obtained from Santa Cruz Biotechnology Corporation (Santa Cruz, USA). MCF-7 cells were obtained from the American Type Culture Collection (ATCC, Manassas, Virginia). Fetal bovine serum (FBS) was obtained from Gibco Laboratories (NY, USA), and doxorubicin (DOX) was obtained from HVSSF United Chemical Materials Co., Ltd. (Beijing, China).

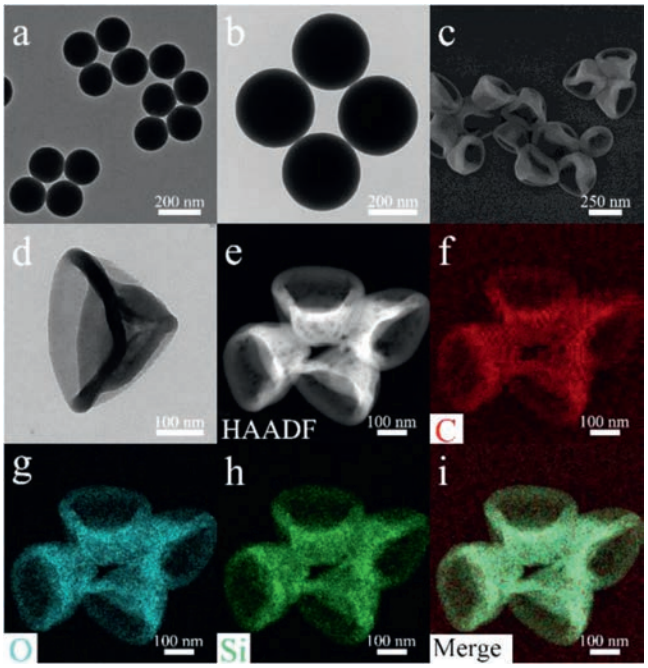

Fig. 1. TEM image of MONs synthesized through the surfactant-directed sol-gel process by adding silane precursors (a) one time and (b) two times. (c) SEM and (d) TEM images of DDHMONs prepared by multi-interfacial alkaline (NaOH) etching. (e) STEM-HAADF image and (f-i) EDX elemental mapping images of DDHMONs.

The DDHMONs were synthesized as follows: First, 0.08 g of CTAB was dissolved in a mixture containing deionized water (37.5 mL) and ethanol (15 mL) together with concentrated ammonia (25 wt%, 0.5 mL). The above mixed solution was placed in an environment at 35 °C and stirred at 1100 rpm for 1 h, and then BTSE (0.02 mL) and TEOS (0.0675 mL) were added. After stirring for 24 h, MONs were collected by centrifugation and then washed with ethanol. Subsequently, 0.16 g of CTAB was dissolved in a mixture containing 75 mL of deionized water, 30 mL of ethanol and 1.0 mL of ammonia solution, and then the collected MONs were redispersed in the reaction solution. Afterward, a blend of BTSE (0.1 mL) and TEOS (0.15 mL) was added. After another 24 h of stirring, MONs with the silane precursors added twice during the synthesis process were collected. Next, the MONs were distributed again in 30 mL of water and etched by a sodium hydroxide solution (5 mol/L, 3.75 mL) for 15 min. Finally, after washing three times with water, the CTAB template was extracted twice at 60 °C in a mixed solution of concentrated hydrochloric acid (400 μL, 37%) and ethanol (240 mL) for 3 h. When the CTAB surfactant was removed, the product was washed with ethanol twice, and double-shell deformable hollow mesoporous organosilica nanocapsules were obtained.

After completing the synthesis of DDHMONs, the following instruments were employed for material characterization. A Hitachi HT7700 microscope was used to obtain transmission electron microscopy (TEM) images. A Hitachi S4800 microscope was employed to obtain scanning electron microscopy (SEM) images. High-resolution transmission electron microscopy (HR-TEM) and elemental distribution results were obtained *via* an FEI Talos F200X electron microscope with energy-dispersive X-ray (EDX) spectroscopy. Hydrodynamic dimensions and zeta potentials were measured using a Brookhaven Zeta PALS analyzer. A Nicolet NEXUS870 spectrometer was employed to obtain Fourier transform infrared (FT-IR) spectra. A Bruker AVANCE III400 spectrometer was employed to obtain ^{29}Si magic angle rotation (MAS) NMR spectra. A Micromeritics ASAP 2020 analyzer was employed to obtain nitrogen adsorption-desorption isotherms. Specific surface areas were obtained by utilizing the adsorption data with relative pressures (P/P_0) of 0.05 to 0.21 through the Brunauer-Emmett-Teller (BET) method. The material was degassed at 150 °C under vacuum for 12 h. The pore size distribution was calculated from the isotherm adsorption branch by employing the nonlocal density functional theory (NLDFT) method.

Because the DDHMONs is negatively charged in physiological solution, so we used the DDHMONs to load positively charged anticancer drug DOX *via* electrostatic interaction. DDHMONs were dispersed in a PBS solution containing DOX (1 mg/mL). The centrifuge tube was wrapped with tin foil to block outside light. After shaking for 12 h, the DOX-loaded DDHMONs (DDHMONs-DOX) were gathered through centrifugation and then washed with PBS six times. The loading rate of the drug could be calculated by measuring the free DOX in the supernatant after each centrifugation. Then, we conducted a drug release test by dispersing one milligram of the collected DDHMONs-DOX in one milliliter of PBS with pH values of 5.0 or 7.4. After they were shaken at 35 °C for a certain period of time, the absorbance of the collected supernatant was measured at 490 nm to calculate the drug release rate.

In order to determine the biosafety of the DDHMONs, *in vitro* cytotoxicity test was implemented. First, MCF-7 human breast cancer cells were grown in RPMI 1640 culture medium with FBS (10%) and penicillin-streptomycin (1%). Then, the MCF-7 cells were

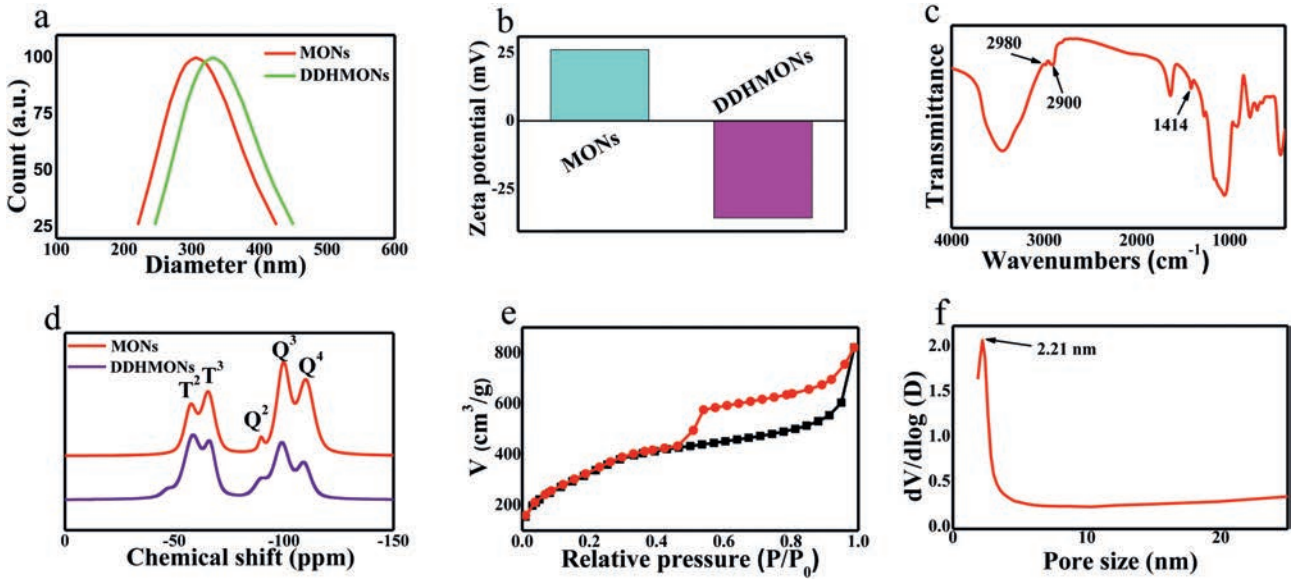

Fig. 2. (a) DLS curve and (b) zeta potential of MONs and DDHMONs. (c) FT-IR of DDHMONs. (d) ^{29}Si MAS NMR spectra of MONs and DDHMONs. (e) Nitrogen adsorption–desorption isotherms of DDHMONs. (f) Pore size distribution curve of DDHMONs synthesized through the multi-interfacial etching approach.

transferred to a 96-well plate at a concentration of 1×10^5 mL^{-1} to continue incubation. After 24 h, various concentrations of DDHMONs were added to each well with the cells. After further incubation for another 24 h, the culture solution was aspirated and replaced with a culture solution containing 10 μL of CCK-8 solution. After the last 2 h of incubation, a microplate reader was used to determine cell vitality.

After confirming the biosafety, we studied the cell uptake of the DDHMONs. First, 1 mL of MCF-7 cells was seeded in a 12-well plate, and then different components, including 20 μg of free DOX, DDHMONs-DOX loaded with 20 μg of DOX and DDHMONs without DOX (the quality was the same as the DDHMONs part of the DDHMONs-DOX), were added to the culture medium. After incubating for 2, 6 and 12 h, the cells were washed with PBS and dispersed in 1 mL of PBS so that a flow cytometer could be used to determine the respective cell uptake rate. In addition, after the above steps, the MCF-7 cells could be immobilized by paraformaldehyde and stained with DAPI for nuclear quantitation. These stained cells could be viewed on a TSC SP8 confocal laser scanning microscope to obtain confocal images to more intuitively display the cell uptake of free DOX and DDHMONs-DOX.

Finally, we studied the lethality of the DDHMONs-DOX on MCF-7 cells. MCF-7 cells at a density of 1×10^5 cells per milliliter were transferred to unused 96-well plates and incubated for 24 h. Subsequently, DDHMONs-DOX or free DOX that had been decentralized in 100 μL of RPMI 1640 medium at different DOX concentrations were added. After another 24 h or 48 h, the culture medium was aspirated from the 96-well plate and replaced with 100 μL of 10% CCK-8 solution. After another 2 h, the entire 96-well plate was placed in a microplate reader to measure absorbance (490 nm).

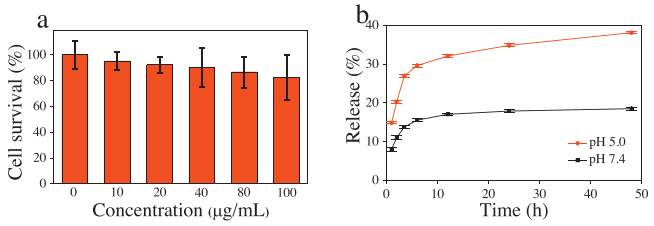

Fig. 3. (a) *In vitro* cell survival rate of MCF-7 cells after incubation with disparate concentrations of DDHMONs for 24 h. (b) Drug release curves of DDHMONs-DOX under acidic (pH 5.0) and neutral (pH 7.4) conditions for 48 h.

MONs are synthesized through a surfactant-directed sol-gel process by adding the silane precursor TEOS together with BTSE in an aqueous ethanol solution. Fig. 1a shows the image of nanospheres obtained by a single addition of silane precursors, thus demonstrating the successful synthesis of MONs with a diameter of 180 nm. With the second addition of coprecursors and reacting for another 24 h, the morphology of the resulting products still maintains a uniform sphere, and their average diameter is approximately 300 nm (Fig. 1b). The results from the elemental mapping images and the elemental line sweep of MONs confirm that the interrelated elements are evenly distributed throughout the spherical structure (Fig. S1 in Supporting information). The surface of both shells becomes soft and shrinks inward after etching in an aqueous sodium hydroxide solution (5 mol/L) for 15 min. Finally, the two shells of the MONs collapse inward, forming double-shelled hollow nanospheres with obvious folds on the surface (Figs. 1c and d). Images from scanning transmission electron microscopy in a high-angle annular dark field (STEM-HAADF) further confirm that these DDHMONs possess a double-shelled hollow structure (Fig. 1e), and both shells are soft and have shrunk inward. The corresponding elemental mapping images of the DDHMONs show that C, O, and Siare homogeneously deposited throughout the solid spheres and soft spheres (Figs. 1f–i), suggesting that the various elements in DDHMONs are still uniformly distributed on the collapsed structure after sodium hydroxide etching. The reason for the formation of this structure is that the less condensed organosilica core and layer between the two shells are totally etched away,thus deforming either of the two shells inwardly due to internal van der Waals forces.

To further verify that the DDHMONs have a double-shelled hollow structure and a soft framework, we compared the nanosphere images from the elemental line scans before and after etching (Fig. S2 in Supporting information). The signal intensity of each element increases uniformly from the position at 50–200 nm and decreases uniformly at the positions of 200 nm and 350 nm, indicating that the synthesized MONs possess a good spherical morphology (Fig. S2a). After scanning DDHMONs, we obtain a different result: the signal intensity of each element at the

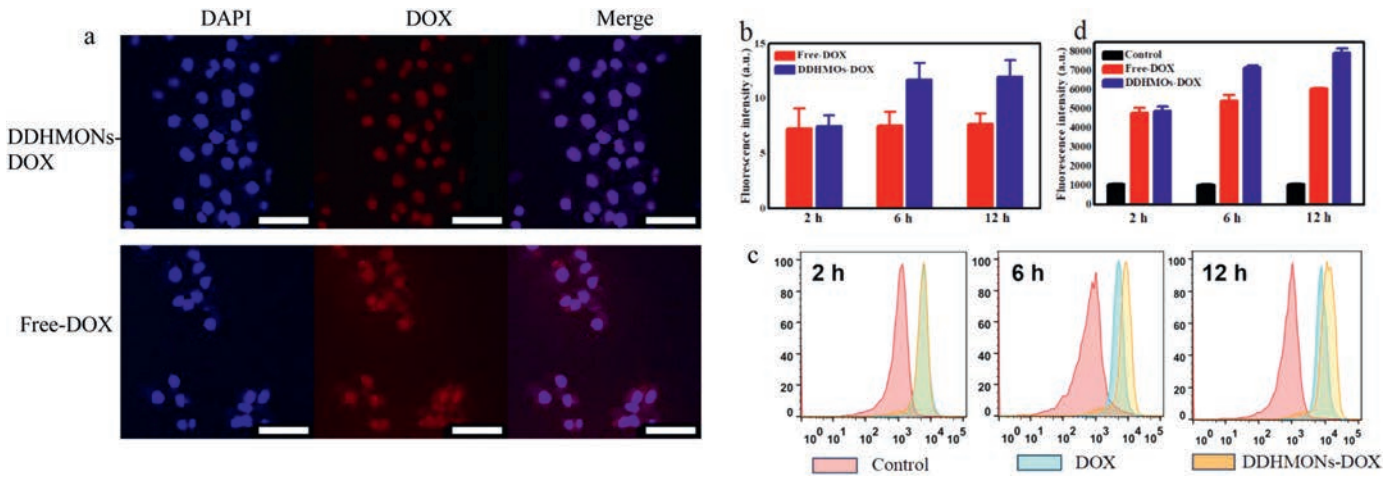

Fig. 4. (a) CLSM images and (b) corresponding fluorescence intensity of MCF-7 cells after the incubation with DOX or DDHMONs-DOX for 12 h. Scale bar: 75 μm. (c) Flow cytometry and (d) corresponding fluorescence intensity of MCF-7 cells after incubation with DOX or DDHMONs-DOX for 2, 6 and 12 h.

initial position of the elemental line scan is several times higher than that at the end (Fig. S2b). This result can be explained as follows: after the sodium hydroxide etching procedure, the organosilica species between the two shells is removed, so the outer shell collapses and squeezes the inner hollow organosilica sphere to one side of the cavity. The above finding further indicates that the DDHMONs were synthesized successfully.

We then individually measured the hydrodynamic diameters and zeta potential of the MONs and DDHMONs. The hydrodynamic diameters of the MONs and DDHMONs are approximately 300 nm and 328 nm, respectively (Fig. 2a). The MONs and DDHMONs have a narrow polydispersity index (PDI) of 0.121 ± 0.02 and 0.129 ± 0.02, demonstrating their excellent dispersity in aqueous solution. The zeta potential of the DDHMONs is -35.6 ± 0.7 mV (Fig. 2b). The FT-IR spectra of DDHMONs show two peaks at 2900 and 2980 cm^{-1}, assigned to the stretching vibration of the C—H bond in the $—CH_2—CH_2—$ part (Fig. 2c), thus manifesting an ethane-bridged framework. In addition, C—H bond signals can be found at 1414 cm^{-1}, further demonstrating its bending vibration. We then employed ^{29}Si MAS NMR to further compare the composition of MONs and DDHMONs. The ^{29}Si MAS NMR spectrum of DDHMONs displays T^2 ($C–Si(OSi)_2(OX)$) and T^3 ($C–Si(OSi)_3$) signals –57 and –68 ppm, respectively (Fig. 2d). The existence of T signals effectively proves that the frameworks of DDHMONs are successfully incorporated with organic groups. In addition, the ^{29}Si MAS NMR spectrum of DDHMONs displays the Q^2 ($Si(OSi)_2(OX)_2$), Q^3 ($Si(OSi)_3(OX)$), and Q^4 ($Si(OSi)_4$) signals at –93, –102 and –112, respectively. It is calculated that the $T^n/(T^n + Q^m)$ ratio of DDHMONs is 0.622, which is remarkably higher than that of MONs (0.395). These results indicate that a large amount of Q silicate species was dissolved after etching with the NaOH aqueous solution. Furthermore, the nitrogen sorption isotherms of DDHMONs reveal a typical IV curve with a hysteresis loop (Fig. 2e), indicating their typical mesoporous structure. In addition, the superficial area and pore volume of DDHMONs are measured as 1234 m^2/g and 1.1 cm^3/g, respectively. Through the NLDFT method, the pore size of DDHMONs is 2.21 nm (Fig. 2f).

To further explore the morphological change in MONs, we next studied the morphology of DDHMONs obtained by the multi-interfacial etching approach. Initially, MONs possessed a uniform spherical shape (Fig. S3a in Supporting information). After incubating with sodium hydroxide solution for 3 min, the organosilica between the outer shell and inner organosilica sphere is preferentially etched away (Fig. S3b in Supporting information). This is attributed to the MONs having more stable outer and inner shells and the core area being too deep for OH^- to reach. Prolonging the etching time from 3 min to 6 min and then to 9 min, the outer solvated shell starts to wrinkle inward, making the cavity between the inner organosilica sphere and the outer shell more obvious (Figs. S3c and d in Supporting information). Then, the inner core section begins to be etched, and another cavity appears when the etching time is increased to 12 min (Fig. S3e in Supporting information). At 15 min, all the sections except the inner and outer shells are completely etched, and the remaining two shells collapse inward to form a deformable double-shelled hollow structure (Fig. S3f in Supporting information). For the MONs we obtained, the condensation degree of organosilica in the interior is lower than that of organosilica on the outer surface, thus demonstrating prioritized etching of the interior. Therefore, when the obtained MONs are scattered in NaOH, a cavity forms inside because the original interior is preferentially dissolved by the OH^- attack. Over time, the inorganic silica on the outer shell is further dissolved by OH^-, at which point the framework contains more organic silica components. Organosilica componentsin structures are usually flexible, so when they become the main components of the overall structure after the relatively stable $Si–(O)_4$ is preferentially dissolved, the whole shell of MONs starts to wrinkle inward as a result of van der Waals forces. The MONs we generated can be divided into two parts, namely, the inner organosilica sphere and the outer organosilica shell. Both of them share the same abovementioned etching mechanism. Due to the position of the inner organosilica sphere, the deformation time will be later than that of the outer shell.

Because of the double-shelled structure, when MONs are etched by sodium hydroxide solution, the outer part that is obtained by the second addition of organosilica precursors tends to provide similar protection to the inner part of the structure, making the inner organosilica sphere more difficult to etch. Therefore, we adjusted the ratio of the initially added organosilica/silica precursors (Fig. S4). Under the premise of maintaining a constant total amount of added organosilica precursors, it can be observed that as the proportion of organosilica added for the first time increases, the interior becomes more difficult to etch away.

Then, we studied the biocompatibility of DDHMONs. As shown in Fig. 3a, the survival rate of MCF-7 cells remains over 80% after incubation with DDHMONs at concentrations up to 100 μg/mL for a whole day, indicating that good biocompatibility is a trait of the synthesized DDHMONs. This feature makes DDHMONs suitable for further biomedical applications. Then, DOX, a drug that acts on DNA and has been widely used in chemotherapy, was loaded into

the DDHMONs to form a system for loading and transporting anticancer drugs. It has been determined that the amount of DOX that can be loaded per milligram of DDHMONs is 33.5 mg. Next, the release of DOX loaded in DDHMONs was tested under different pH values within 48 h. During the 0–10 h phase of the experiment, the drug release curve of DDHMONs-DOX shows a significant increase under both acidic and neutral conditions. However, the release rate of DDHMONs-DOX under acidic conditions is significantly higher than that under neutral conditions (Fig. 3b). When the experiment is carried out for 48 h, the calculated drug release percentages under acidic and neutral conditions are 38.9% and 18.4%, respectively. The release characteristic of DDHMONs-DOX under acidic conditions is beneficial for releasing drugs in tumor areas with an acidic microenvironment.

Then, confocal laser scanning microscopy (CLSM) was used to further observe the delivery of DOX in cells. The intracellular fluorescence of cells incubated with DDHMONs-DOX is obviously stronger than that of the free-DOX group, as shown by the CLSM images (Fig. 4a). In detail, the mean intracellular fluorescence intensity of MCF-7 cells after incubation with DDHMONs-DOX for 12 h is measured to be 11.99 (Fig. 4b), approximately 1.6 times that of the free-DOX group (7.52). Furthermore, the cellular uptake efficiencies of DDHMONs-DOX and the free-DOX group were quantitatively investigated by flow cytometry. Whether under 6 h or 12 h, the flow cytometry results reveal that MCF-7 cells incubated with DDHMONs-DOX show significantly enhanced fluorescence compared with those treated with the free-DOX group (Fig. 4c). This result demonstrates that the ability of DDHMONs to deliver DOX into MCF-7 cells is more efficient than that of the free-DOX group. In addition, the relative average fluorescence intensities of the DDHMONs-DOX-treated group are 7260 and 7967 after incubation for 6 and 12 h (Fig. 4d), respectively, both of which are up to 1.4 times the fluorescence intensity of the free-DOX group (5211 and 5832, respectively). These results strongly confirm that the DOX loading in DDHMON carriers is more efficiently taken in by MCF-7 cells than that is the free-DOX group. The high drug delivery efficiency for the DDHMONs is attributed to that the DDHMONs can deliver DOX into cells *via* endocytosis and decrease their excretion. In addition, the deformable characteristic of the DDHMONs make them easier to be taken up by cells compared to hard particles [36].

Finally, the effect of DDHMONs-DOX on MCF-7 cell chemotherapy was tested. (Fig. S5 in Supporting information). As the concentration of DOX increases, the viability of MCF-7 cells gradually decreases. The cell viability decreases to 55.2% as the concentration of free DOX increases to 160 μg/mL 24 h later. If we extended the incubation to 48 h, the cell vitality can be further reduced to 36.1%. Notably, when we incubated cells with DDHMONs-DOX, the 24-h and 48-h survival rates of the cells are further reduced to 50.4% and 14.9%, respectively. This result suggests that compared with the free-DOX group, DDHMONs-DOX have better cancer cell killing capability.

In summary, we successfully synthesized deformable double-shelled hollow mesoporous organosilica spheres (DDHMONs) by a multi-interfacial etching strategy. The obtained DDHMONs possess a unique deformable double-shelled structure with a highly uniform outer layer diameter (~320 nm) and inner layer diameter (~180 nm), ordered mesochannels (~2.21 nm), a high specific surface area (~1233 m^2/g) and excellent biocompatibility. In addition, the DDHMONs have a good anticancer drug (DOX) payload capacity (~335 μg/mg) together with pH-sensitive release characteristics. The relevantCLSM and flow cytometry data indicate that the DDHMONs have the ability to effectively deliver DOX into MCF-7 cells. Furthermore, compared with the free-DOX group, DDHMONs-DOX have a higher cancer cell killing ability, thus showing their potential application in nanomedicine.

Declaration of competing interest

The authors report no declarations of interest.

Acknowledgments

This work was financially supported by the National Key Research and Development Program of China (Nos. 2017YFA0205301, 2017YFA0205302), the Key Research and Development Program of Jiangsu (No. BE2018732), the National Natural Science Foundation of China (Nos. 81971675, 21603106), the Natural Science Foundation of Jiangsu Province (No. BK20160017) and the State Key Laboratory of Analytical Chemistry for Life Science (No. 5431ZZXM1717).

Appendix A. Supplementary data

Supplementary material related to this article can be found, in the online version, at doi:https://doi.org/10.1016/j.cclet.2020.08.023.

References

[1] Z. Teng, X. Su, Y. Zheng, et al., J. Am. Chem. Soc. 137 (2015) 7935–7944.
[2] Y. Chen, Q. Meng, M. Wu, et al., J. Am. Chem. Soc. 136 (2014) 16326–16334.
[3] X. Li, L. Zhou, Y. Wei, et al., J. Am. Chem. Soc. 137 (2015) 5903–5906.
[4] P. Huang, X. Qian, Y. Chen, et al., J. Am. Chem. Soc. 139 (2017) 1275–1284.
[5] Schacht, S. Huo, Q. Voigt-Martin, I.G. Stucky, G.D. Schüth, Science 273 (1996) 768–771.
[6] B. Wang, J. Chen, H. Wu, Z. Wang, X. Lou, J. Am. Chem. Soc. 133 (2011) 17146–17148.
[7] Z. Teng, G. Zheng, Y. Dou, et al., Angew. Chem. Int. Ed. 51 (2012) 2173–2177.
[8] Z. Teng, S. Wang, X. Su, et al., Adv. Mater. 26 (2014) 3741–3747.
[9] H. Chen, C. Yuan, X. Yang, et al., ACS Appl. Nano Mater. 3 (2020) 4586–4598.
[10] X. Yang, P. Lu, L. Yu, et al., Adv. Funct. Mater. (2020) 2002488.
[11] X. Cheng, H. Zhao, W. Huang, et al., Langmuir 34 (2018) 7663–7672.
[12] Z. Li, Y. Wang, A.A. Elzatahry, et al., Chin. Chem. Lett. 31 (2020) 1598–1602.
[13] J. Liu, N.P. Wickramaratne, S. Qiao, M. Jaroniec, Nat. Mater. 14 (2015) 763–774.
[14] Y. Liu, A.A. Elzatahry, W. Luo, et al., Nano Energy 25 (2016) 80–90.
[15] L. Zhang, H. Wu, X. Lou, J. Am. Chem. Soc. 135 (2013) 10664–10672.
[16] P. Xu, R. Yu, H. Ren, et al., Chem. Sci. 5 (2014) 4221–4226.
[17] Z. Dong, X. Lai, J.E. Halpert, et al., Adv. Mater. 24 (2012) 1046–1049.
[18] Z. Dong, H. Ren, C.M. Hessel, et al., Adv. Mater. 26 (2014) 905–909.
[19] G. Zhu, F. Zhang, X. Li, et al., Angew. Chem. Int. Ed. 58 (2019) 6669–6673.
[20] L. Yu, P. Pan, Y. Zhang, et al., Small 15 (2019) 1805465.
[21] G. Sun, F. Zhang, Q. Xie, W. Luo, J. Yang, Chin. Chem. Lett. 31 (2020) 1603–1607.
[22] G. Zhu, R. Guo, W. Luo, et al., Natl. Sci. Rev. 2 (2020), doi:http://dx.doi.org/10.1093/nsr/nwaa152.
[23] C. Wei, H. Fei, Y. Tian, et al., Chin. Chem. Lett. 31 (2020) 980–983.
[24] Y. Wong, L. Zhu, W. Teo, et al., J. Am. Chem. Soc. 133 (2011) 11422–11425.
[25] D. Gu, H. Bongard, Y. Meng, et al., Chem. Mater. 22 (2010) 4828–4833.
[26] W. Cho, Y.H. Lee, H.J. Lee, M. Oh, Adv. Mater. 23 (2011) 1720–1723.
[27] S.H. Hwang, D.H. Shin, J. Yun, et al., Chem. Eur. J. 20 (2014) 4439–4446.
[28] X.W. Lou, C. Yuan, L.A. Archer, Small 3 (2007) 261–265.
[29] X. Yi, X. Shi, H. Gao, Phys. Rev. Lett. 107 (2011) 098101.
[30] T. Asefa, M.J. MacLachlan, N. Coombs, G.A. Ozin, Nature 402 (1999) 867–871.
[31] P. Van Der Voort, D. Esquivel, E. De Canck, et al., Chem. Soc. Rev. 42 (2013) 3913–3955.
[32] H. Sun, E.H.H. Wong, Y. Yan, et al., Chem. Sci. 6 (2015) 3505–3514.
[33] X. Su, J. Tao, Q. Wang, et al., Chin. Chem. Lett. 30 (2019) 929–932.
[34] X. Su, J. Tao, S. Chen, et al., Chin. Chem. Lett. 30 (2019) 1089–1092.
[35] J. Key, A.L. Palange, F. Gentile, et al., ACS Nano 9 (2015) 11628–11641.
[36] Z. Teng, C. Wang, Y. Tang, et al., J. Am. Chem. Soc. 140 (2018) 1385–1393.